JOURNAL OF THE ROYAL SOCIETY Interface

rsif.royalsocietypublishing.org

Research

Cite this article: Carnelli D, Vena P, Dao M, Ortiz C, Contro R. 2013 Orientation and size-dependent mechanical modulation within individual secondary osteons in cortical bone tissue. J R Soc Interface 10: 20120953. http://dx.doi.org/10.1098/rsif.2012.0953

Received: 20 November 2012
Accepted: 11 January 2013

Subject Areas:
biomechanics

Keywords:
hierarchical structure, anisotropy, length-scale effect, nanoindentation, secondary osteons

Author for correspondence:
Davide Carnelli
e-mail: davide.carnelli@mat.ethz.ch

†Present Address: Complex Materials, Department of Materials, ETH Zürich, Wolfgang-Pauli-Strasse 10, 8093 Zürich, Switzerland.

Royal Society Publishing
Informing the science of the future

Orientation and size-dependent mechanical modulation within individual secondary osteons in cortical bone tissue

Davide Carnelli[1,3,†], Pasquale Vena[2,4], Ming Dao[3], Christine Ortiz[3] and Roberto Contro[1]

[1]Department of Structural Engineering, and [2]Department of Chemistry, Material and Chemical Engineering, LaBS-Laboratory of Biological Structure Mechanics, Politecnico di Milano, P.zza L. da Vinci 32, 20133 Milan, Italy
[3]Department of Materials Science and Engineering, Massachusetts Institute of Technology, 77 Massachusetts Avenue, Cambridge, MA 02139, USA
[4]IRCCS, Istituto Ortopedico Galeazzi, P.zza R. Galeazzi 4, 20161 Milano, Italy

Anisotropy is one of the most peculiar aspects of cortical bone mechanics; however, its anisotropic mechanical behaviour should be treated only with strict relationship to the length scale of investigation. In this study, we focus on quantifying the orientation and size dependence of the spatial mechanical modulation in individual secondary osteons of bovine cortical bone using nanoindentation. Tests were performed on the same osteonal structure in the axial (along the long bone axis) and transverse (normal to the long bone axis) directions along arrays going radially out from the Haversian canal at four different maximum depths on three secondary osteons. Results clearly show a periodic pattern of stiffness with spatial distance across the osteon. The effect of length scale on lamellar bone anisotropy and the critical length at which homogenization of the mechanical properties occurs were determined. Further, a laminate-composite-based analytical model was applied to the stiffness trends obtained at the highest spatial resolution to evaluate the elastic constants for a sub-layer of mineralized collagen fibrils within an osteonal lamella on the basis of the spatial arrangement of the fibrils. The hierarchical arrangement of lamellar bone is found to be a major determinant for modulation of mechanical properties and anisotropic mechanical behaviour of the tissue.

1. Introduction

Cortical bone is a heterogeneous, hierarchical composite material with important structural features spanning multiple length scales, each of which contributes to macroscopic biomechanical function [1–5]. At the microstructural level, both in humans and in many other large vertebrates, a particularly critical determinant of the mechanical properties of the whole tissue are concentric lamellar cylindrical structures called secondary osteons (figure 1*a–c*) [6,7].

The detailed lamellar structure within individual secondary osteons was interrogated via synchrotron X-ray texture measurements and consists of three-dimensional helicoids of mineralized collagen fibrils [6]. Transmission electron microscopy [7–10] revealed that the mineralized collagen fibrils that make up one sub-layer of the lamellar unit have an internal crystalline structure. Within each lamella, which typically has a approximately 3–7 μm thickness, the long axis of the collagen fibrils rotates from a direction roughly parallel to the osteonal axis at one lamellar boundary (referred to as 'thick' sub-layers or sub-lamellae, approx. 2–4 μm thick) to a direction approximately perpendicular to it at the opposite lamellar boundary (referred to as 'thin' sub-layers or sub-lamellae, approx. 1–2 μm thick.

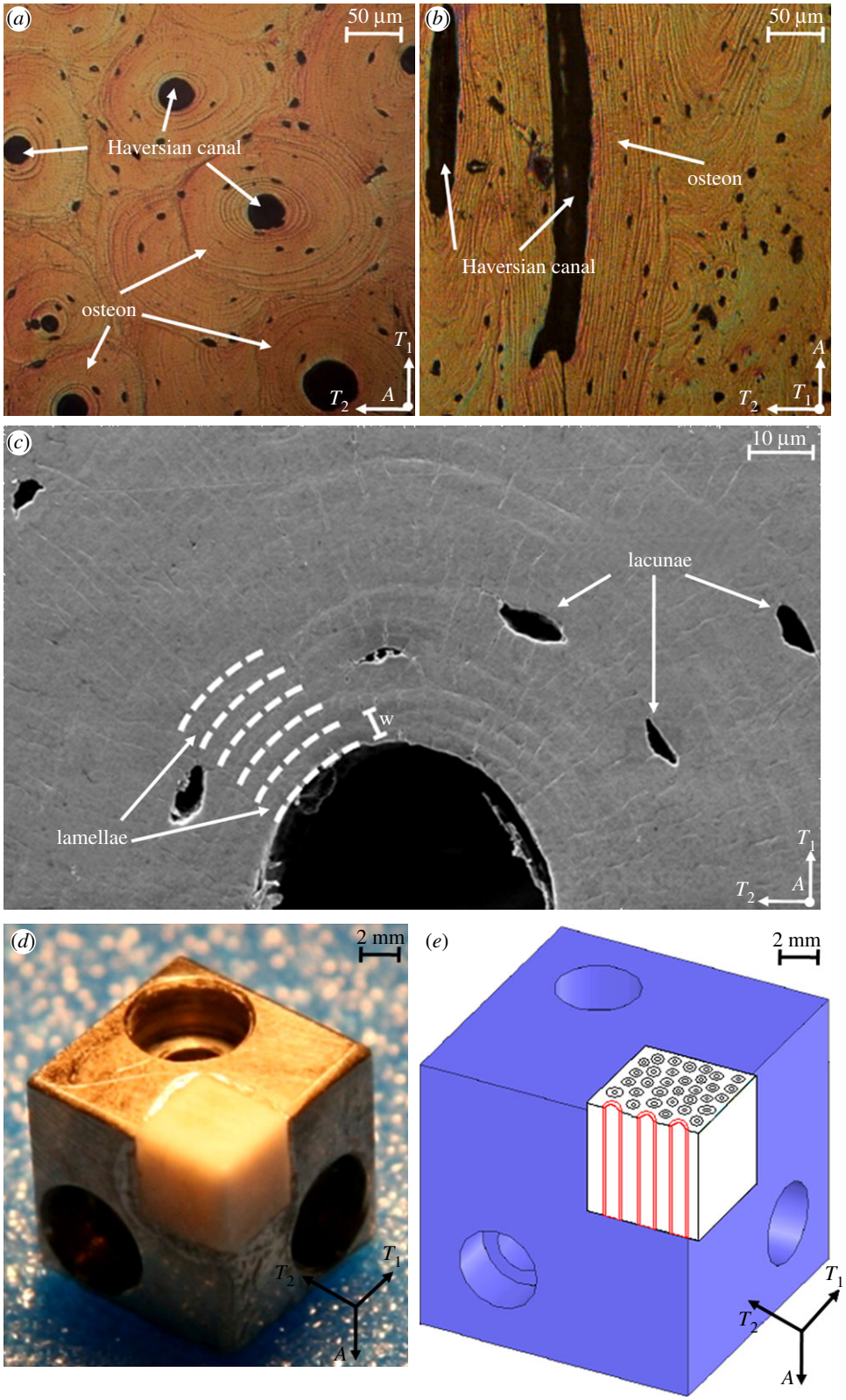

Figure 1. (*a*) Optical microscopy image of osteonal bovine bone tissue parallel to the osteonal axis (axial direction). (*b*) Optical microscopy image of osteonal bovine bone tissue normal to the osteonal axis (transverse direction). (*c*) Scanning electron microscopy image of a region surrounding an individual osteon parallel to the osteonal axis. (*d*) Home-built sample stage enabling the testing of two orthogonal orientations within the same osteon. (*e*) Illustration of the indentation test directions (A and T_1) with respect to the osteonal microstructure (in red). (Online version in colour.)

The mechanical characterization of individual osteons was performed in tension, compression and torsion [11–13], as well as with ultrasound [14]. Instrumented indentation was also applied to evaluate the elastic properties of lamellar bone within the osteonal structure along multiple orientations [15–17]. These studies identified anisotropic elasticity of individual osteons, where the axial direction was stiffer than the transverse direction with an anisotropic ratio (axial/transverse) of approximately 1.5, similar to the value found for macroscopic cortical bone [2,3] and lower than the expected value for individual mineralized collagen fibrils (approx. 2.0) [18].

Table 1. Nomenclature.

A	axial indentation direction w.r.t. the global coordinate system
A, T_1, T_2	global coordinate system (osteons)
a_1, a_2	semi-axes lengths of the elliptical projected area of contact
$\mathbf{a_1}$, $\mathbf{a_2}$, $\mathbf{a_3}$	indentation coordinate system for the Swadener–Pharr model
$\mathbf{B}$	Barnett–Lothe tensor
$\mathbf{C}$	stiffness tensor
C_{ijhk}	stiffness tensor coefficients
E	uniaxial Young's modulus
E_L	uniaxial Young's modulus along the mineralized collagen fibrils long axis direction
E_P	uniaxial Young's modulus perpendicular to the mineralized collagen fibril long axis for a transversely isotropic material model
E_{P1}, E_{P2}	uniaxial Young's moduli perpendicular to the mineralized collagen fibril long axis for an orthotropic material model
G_{LP}	shear modulus for a mineralized collagen fibril in the $L-P$ plane for a transversely isotropic material model
G_{LP1}, G_{LP2}, G_{P1P2}	shear moduli for a mineralized collagen fibril in the $L-P_1$, $L-P_2$ and P_1-P_2 planes for an orthotropic material model
L	longitudinal indentation direction w.r.t. the local coordinate system
L, P_1, P_2	local coordinate system (mineralized collagen fibrils)
M	indentation modulus
M_A	indentation modulus in the axial direction
M_T	indentation modulus in the transverse direction
M_0	oscillatory function mean value
M^{exp}	experimental indentation modulus
M^{comp}	indentation modulus computed with the Swadener–Pharr method
P	perpendicular indentation direction w.r.t. the local coordinate system
T	transverse indentation direction w.r.t. the global coordinate system
r	radial position across the osteon
r_i	locations corresponding to the peaks and valleys of the stiffness modulation in the axial and transverse directions
$\mathbf{r}$, $\mathbf{s}$, $\mathbf{t}$	orthogonal reference system for the Swadener–Pharr model
w	lamellar width
γ	angle between the direction $\mathbf{t}$ and the $\mathbf{a_1}$ axis
ΔM	oscillatory function amplitude
θ	angle between the long axis of the mineralized collagen fibrils and the loading direction
ν_{LP}, ν_{PP}	Poisson's ratios for a mineralized collagen fibril in the $L-P$ and perpendicular ($P-P$) planes for a transversely isotropic material model
ν_{P1L}, ν_{P2L}, ν_{P2P1}, ν_{LP1}, ν_{LP2}, ν_{P1P2}	Poisson's ratios for a mineralized collagen fibril in the $L-P_1$, $L-P_2$ and P_1-P_2 planes for an orthotropic material model

Considering the hierarchical structural features of bone [6], different characteristic sizes which may also play functional roles in bone exist at different length scales [19–21]. In a recent study, Yao *et al.* [21] adopted AFM-based nanoindentation to identify a characteristic length scale of approximately 200 nm within one sub-layer of the lamellar unit; at a higher level, spatially controlled nanoindentation experiments within individual osteons allowed Gupta *et al.* [19] to identify a larger characteristic length scale owing to the periodicity of the osteonal lamellae, with thicker sub-lamellae of higher stiffness alternating with thinner sub-lamellae of lower stiffness. The spatial variation of indentation modulus within a lamella was attributed to the rotation of the inherently anisotropic collagen fibrils [19,22] and variations in the mineral content [19]. Nevertheless, an experimentally validated analytical model that directly links the nano-scale rotational arrangements of collagen fibrils and the corresponding anisotropic elasticity is still missing.

In this study, we focus on quantifying the orientation and size dependence of the spatial mechanical modulation in individual secondary osteons of bovine cortical bone using nanoindentation. Experiments were carried out in two orthogonal orientations within the same individual osteon. Tests were performed at four different maximum penetration depths to study the effect of indentation area on mechanical modulation. An analytical model that assumes the inherent anisotropy of the mineralized collagen fibrils as well as their orientation was introduced to estimate the elastic constants of a sub-layer of mineralized collagen fibrils.

2. Material and methods

In the following, the Haversian canal axis is referred to as the 'axial' direction (A), whereas the plane perpendicular to this axis is referred to as the 'transverse' direction (T_1, T_2). Similarly, the long axis of the mineralized collagen fibrils is herein referred to as the 'longitudinal' direction (L), while the plane perpendicular to this axis is referred to as the 'perpendicular' direction (P_1, P_2). Thus, A, T_1, T_2 represents a global coordinate system based on the whole secondary osteon; whereas, L, P_1, P_2 represents a local coordinate system related to the mineralized collagen fibrils (table 1).

2.1. Sample preparation and characterization

Samples were kept under conditions close to the physiological one until the tests; to this purpose no alcohol dehydration, freezing, embedding, thermal drying, long-term storage in ambient conditions or chemical fixation were used. Adult lamellar bone obtained from a 30 month old cow was harvested from between the tibial metaphysis and diaphysis. Approximately 5 mm cubic specimens were obtained using a diamond-impregnated annular wafering saw (Isomet 5000, Buehler, Inc., Lake Bluff, IL, USA) running at 400–600 r.p.m. under constant water irrigation. In order to expose the osteons' Haversian canal, the first two cuts were performed along the transverse directions and the second ones along the axial directions. The samples were then polished using a metallographic polishing wheel and adhesive papers with successively smaller Al_2O_3 particle grit sizes. Samples were rinsed copiously with de-ionized (DI) water followed by ultrasonication in DI water between polishing intervals. The cutting and polishing procedures were performed the day after harvesting.

From optical (Nikon Eclipse L150, figure 1*a*,*b*) and scanning electron microscopy (JEOL SEM 6320FV, figure 1*c*), the average osteonal diameter was found to be approximately 200 μm and the average thickness of the first four or five individual lamellae around the Haversian canal is 5.01 ± 0.10 μm. Contact mode atomic force microscope (AFM, MFP-3D, Asylum Research, Inc., Santa Barbara, CA, USA) imaging was performed to assess the r.m.s. surface roughness achieved with the polishing procedure, which was quantified as 6.0 ± 0.7 nm on several 2 × 2 μm areas in different locations on the three osteonal structures.

Finally, samples were fixed into the groove of a home-built sample holder that allows for mechanical testing of the same osteonal structure in different directions with respect to the osteonal axis (figure 1*d*,*e*).

2.2. Nanoindentation experiments

All instrumented indentation experiments were conducted in the osteonal region of cortical bone shortly after harvesting and over a short enough time period so that no significant modification of the sample state was ensured; to this purpose the statistical invariance of experimental data over time (the whole time span of the testing period) was checked (data not shown). The effect of hydration state was neglected at this stage, as the bone samples were tested in ambient conditions (20°C and 50% relative humidity). A Triboindenter (Hysitron, Inc., Minneapolis, MN, USA) was used with a Berkovich diamond tip. The tip area function and machine compliance were calibrated on a fused silica reference sample by performing 100 indentations between 100 to 10 000 μN maximum forces [23].

Experiments were performed in displacement control along arrays going radially out from the Haversian canal edge to the external region of the osteon at four different maximum depths: 50, 100, 200 and 300 nm. The experimental procedure is detailed in table 2. The displacement rates of the indentation experiments were 20 and 100 nm s^{-1} in the loading and unloading branches of the indentation curve, respectively. An automatic preliminary thermal drift correction was applied before each indentation. Preliminary investigations were performed to ensure that time-dependent effects were minimal (see [24] for further details). This experimental procedure was used on three secondary osteons in both the axial and transverse directions (A and T_1, respectively, in figure 1*a*–*e*). A total of approximately 2000 indentations were carried out.

Table 2. Summary of the indentation tests carried out in this work. The procedure explained below has been performed in both the axial (A) and transverse (T_1) directions on three secondary osteons.

number of indentations rows × columns	maximum depth (nm)	spacing (μm)
41 × 3	50	0.5
31 × 3	100	1
21 × 3	200	2
21 × 3	300	3

The Oliver–Pharr method [25] was adopted to obtain the indentation modulus M from the unloading portion of each test. An unloading segment range between 95 and 40 per cent of maximum load was chosen for data fitting.

2.3. Empirical formulation for stiffness modulation

The oscillatory function

$$M(r) = \frac{\Delta M}{2}\sin\left(\frac{2\pi r}{w} + c\right) + M_0 \tag{2.1}$$

was adopted to fit the stiffness modulation along the indentation paths. In equation (2.1), r is the radial position across the osteon, $r = 0$ being the Haversian canal inner edge; w is the mean value of the experimentally observed lamellar width (5.01 μm); ΔM is the oscillatory function amplitude; M_0 is its mean value.

2.4. Anisotropic analytical models

The spatial modulation of stiffness at the lowest maximum indentation depth probed (50 nm) was fitted to an analytical model that assumes the inherent anisotropy of the mineralized collagen fibrils and allows for the evaluation of the effective stiffness of the sub-lamellae as a function of collagen fibril orientation. The orientation-dependent uniaxial Young's modulus E of an individual sub-lamella was obtained by applying the rotation formula [19,26,27]

$$E(\theta) = \left[\frac{\cos^4(\theta)}{E_L} + \frac{\sin^4(\theta)}{E_P} + \left(\frac{1}{G_{LP}} - 2\frac{\nu_{LP}}{E_L}\right)\cos^2(\theta)\sin^2(\theta)\right]^{-1}, \tag{2.2}$$

where θ is the angle between the long axis of the mineralized collagen fibrils (longitudinal direction, L) and the loading direction, E_L is the uniaxial Young's modulus along the mineralized collagen fibrils long axis direction (longitudinal direction, L), E_P is the uniaxial Young's modulus perpendicular to the mineralized collagen fibril axis (perpendicular directions, P_1 and P_2), G_{LP} is the shear modulus and ν_{LP} is the Poisson's ratio. The model assumes that individual collagen fibrils and uniformly oriented planar layers of fibrils are transversely isotropic ($P_1 = P_2 = P$) [28–30].

The uniaxial Young's moduli were directly estimated from the experimental nanoindentation loading–unloading curves by using the analytical model for anisotropic elastic contact introduced by Delafargue & Ulm [31]. This model relates the

indentation moduli of the mineralized collagen fibril sub-lamellae in the longitudinal (L) and perpendicular (P_1, P_2) directions to the material stiffness tensor coefficients for individual collagen fibril layers ($C_{ijhk} = C_{ijhk}(E_L, E_P, G_{PL}, \nu_{LP}, \nu_{PP},)$, ν_{PP} being the Poisson's ratio in the isotropy plane). The model holds for transversely isotropic and orthotropic solids under rigid conical indentation along the three principal material symmetry directions. For a transversely isotropic material model, the indentation modulus M in the axis of symmetry direction (here named as direction 3, corresponding to the longitudinal collagen fibril axis direction L) is explicitly related to C_{ijhk} with the following expression:

$$M_3 = 2\sqrt{\frac{C_{1111}C_{3333} - C_{1133}^2}{C_{1111}}\left(\frac{1}{C_{2323}} + \frac{2}{\sqrt{C_{1111}C_{3333}} + C_{1133}}\right)^{-1}}. \tag{2.3}$$

For the indentation directions normal to the axis of symmetry (directions 1 and 2, corresponding to the perpendicular collagen fibril axes direction $P_1 = P_2 = P$), the indentation moduli M_1, M_2 are as follows:

$$M_1 = M_2 \approx \sqrt{\frac{C_{1111}^2 - C_{1122}^2}{C_{1111}}\left(\frac{C_{1111}}{C_{3333}}\right)^{1/2}} M_3. \tag{2.4}$$

The above formulae were applied at those indentation locations for which indentation direction is assumed to be aligned with a principal material direction (i.e. in the case of indentation of thick and thin sub-lamellae). Using the indentation moduli M_1 and M_3 calculated from nanoindentation data via the Oliver–Pharr method, equations (2.3) and (2.4) were solved for E_L and E_P. The Poisson's ratios υ_{LP}, υ_{PP} were assumed according to literature data ([18], see equation (3.1)) and the shear modulus G_{LP} was related to the remaining parameters (see equation (3.1)).

For validation purposes, the Swadener–Pharr method [32] was used to compute the indentation moduli M in all the directions of the space for a given stiffness tensor **C,** as obtained from the solutions of equations (2.2)–(2.4):

$$M = \frac{4\pi}{\int_0^{2\pi} (\mathbf{B}^{-1}(\mathbf{t}(\gamma), \mathbf{C}) : [\mathbf{a}_3 \otimes \mathbf{a}_3] / \sqrt{(a_1/a_2)\cos^2\gamma + (a_1/a_2)\sin^2\gamma}) \mathrm{d}\gamma}. \tag{2.5}$$

In this formulation, **B** is the Barnett–Lothe tensor related to stiffness tensor **C**; (**r**, **s**, **t**) is an orthogonal reference system; ($\mathbf{a_1}$, $\mathbf{a_2}$, $\mathbf{a_3}$) is the indentation coordinate system; γ is the angle between the direction **t** and the $\mathbf{a_1}$ axis; a_1 and a_2 are the semi-axes lengths of the elliptical projected area of contact.

3. Results

3.1. Mechanical modulation at the lamellar level

The average loading–unloading indentation curves obtained in the two orthogonal directions at the four maximum penetration depths are reported in figure 2. The curves show how the indentation response of the tissue depends on the global orientation direction (A versus T). A good repeatability of the loading branch for increasing loads was obtained between tests at different maximum depth. The mean value and standard deviation of maximum load at 50, 100, 200, and 300 nm are 107 ($\pm$10) µN, 326 ($\pm$29) µN, 1004 ($\pm$69) µN, and 1984 ($\pm$104) µN, respectively, in the axial direction, and 110 ($\pm$19) µN, 263 ($\pm$29) µN, 648 ($\pm$77) µN, and 1354 ($\pm$218) µN, respectively, in the transverse direction. The corresponding coefficient of variation (COV, defined as the ratio between the standard deviation and the mean value) ranges between approximately 0.17 (at 50 nm maximum depth, transverse direction) and approximately 0.05 (at 300 nm maximum depth, axial direction). The tissue indentation modulus ranges from 26.24 ($\pm$1.68) GPa to 19.73 ($\pm$0.73) GPa in the axial direction and from 23.59 ($\pm$3.55) GPa to 15.39 ($\pm$1.04) GPa in the transverse direction. The corresponding COV ranges between approximately 0.15 (at 50 nm maximum depth, transverse direction) and approximately 0.04 (at 300 nm maximum depth, axial direction).

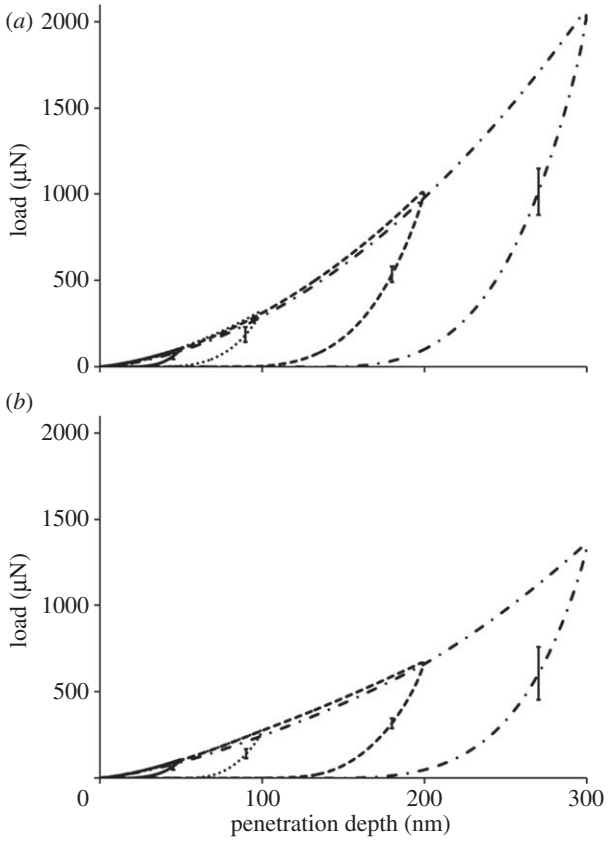

Figure 2. Averaged load versus penetration depth plots in the (*a*) axial and (*b*) transverse directions at the four tested maximum depths. Error bars are $\pm$s.d. calculated at 50% of the maximum load during the unloading curve ($n = 363$ for 50 nm (solid line) maximum depth tests, $n = 273$ for 100 nm (dotted line) maximum depth tests, $n = 189$ for 200 nm (dashed line) and 300 nm (dashed dotted line) maximum depth tests).

The indentation modulus M shows a periodic alternating trend of stiffness with spatial distance radially across the osteon for both the axial (figure 3) and transverse (figure 4) directions, consistent with results reported in Gupta *et al.* [19]. The coefficient of determination (R^2) for fits of the experimental data (figures 3 and 4) to equation (2.1) ranged between 0.61 and 0.01. Higher correlations were found for data taken at the smaller depths (50 nm), whereas smaller values corresponded to indentations carried out at 300 nm depths in both directions. All the obtained R^2 values are reported in the caption of figures 3 and 4. Further, a power analysis has been carried out on the data of figures 3 and 4. A statistically significant difference (one-way ANOVA, $p < 0.001$) was found between the peaks and the valleys of the modulation at 50 and 100 nm maximum depth in both the axial and transverse direction, as well as for the 200 nm, axial direction experiments ($p < 0.05$). Instead, no statistically significant difference ($p > 0.05$) was found at

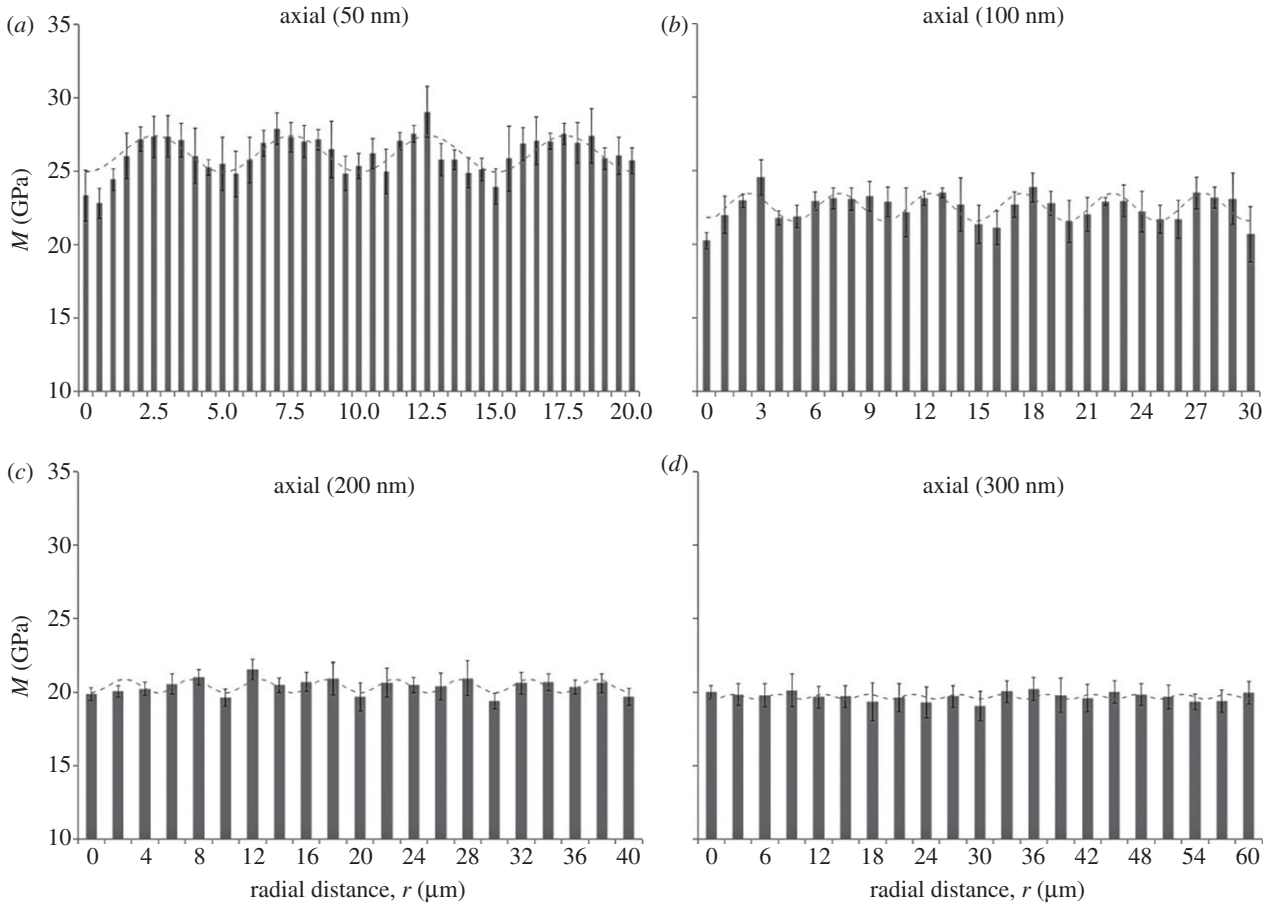

Figure 3. Spatial dependence of indentation modulus at (*a*) 50, (*b*) 100, (*c*) 200 and (*d*) 300 nm maximum penetration depth for axial experiments (parallel to the osteonal axis). Radial distance (r) begins at the Haversian canal edge. Each data point represents the mean value and standard deviation of a total of $n = 9$ measurements. The fitting to the oscillatory function of equation (2.1) is shown in each plot (dashed line). The coefficient of determination (R^2) values are (*a*) 0.60, (*b*) 0.59, (*c*) 0.59 and (*d*) 0.01. Note ordinate does not start at zero.

200 nm maximum depth in the transverse direction and at 300 nm maximum depth.

The mean value, M_0, and the amplitude of the modulation, ΔM, depend on maximum depth and orientation of the indentation tests (figure 5). The mean values M_0 show the tissue to be stiffer when loaded in the axial direction compared with the transverse direction (figure 5*a*): indeed, anisotropy ratios, calculated as axial versus transverse indentation moduli mean values, vary between approximately 1.1 at lower maximum indentation depths (50 and 100 nm) to approximately 1.3 at higher maximum indentation depths (200 and 300 nm). Simultaneously, the spatial modulation of the mechanical properties is higher in the transverse compared with the axial direction (i.e. higher ΔM, figure 5*b*). A decrease in the indentation moduli mean values is observed between 50 and 200 nm maximum depths, this decay being more pronounced in the transverse (approx. 35%) than in the axial (approx. 22%) direction. Instead, no statistically significant difference (one-way ANOVA, $p > 0.05$, $n = 9$) is noticeable within the same direction between 200 and 300 nm (figure 5*a*). The amplitude of the stiffness modulation (figure 5*b*) decreases with the indentation depth as well. The transverse amplitude is approximately two times higher than the axial at 50 nm indentation depth, whereas the trends in the two directions are similar beyond 100 nm depth: indeed, at higher indentation depths (200 and 300 nm), the amplitude values in both directions vanish and the difference between the amplitude values becomes negligible, as the two datasets show no statistically significant difference ($p > 0.05$, $n = 9$).

3.2. Estimation of E_L, E_P and $E(\theta)$ from the anisotropic analytical models

It is expected that carrying out indentations spatially from the Haversian canal edge to the osteonal external boundary will result in the angle θ continuously changing along the radial path owing to the spiral twisting of the mineralized collagen fibrils within a single lamella. E_L and E_P were estimated from indentation data at the lowest maximum indentation depth (50 nm, where both the spatial and depth resolution of the experiments were the highest, figures 3*a* and 4*a*) using the Delafargue & Ulm [31] model. Because this approach is valid only in the principal material symmetry directions, the analysis was carried out at spatial locations across the osteon where the indentation loading axis was parallel and perpendicular to the mineralized collagen fibrils long axis, that is at the nine different points r_i (with $r_i = 0$, 2.5, 5, 7.5, 10, 12.5, 15, 17.5 and 20 μm radial distances from the Haversian canal edge) corresponding to the peaks and valleys of the stiffness modulation in the axial and transverse directions (figures 3*a* and 4*a*). Thus, the indentation moduli $M_A(r_i)$ and $M_T(r_i)$ estimated from the Oliver–Pharr method represent the left-hand side of the system of equations (2.3)–(2.4). In order to simultaneously calculate the uniaxial elastic moduli $E_L(r_i)$ and $E_P(r_i)$, the three remaining material

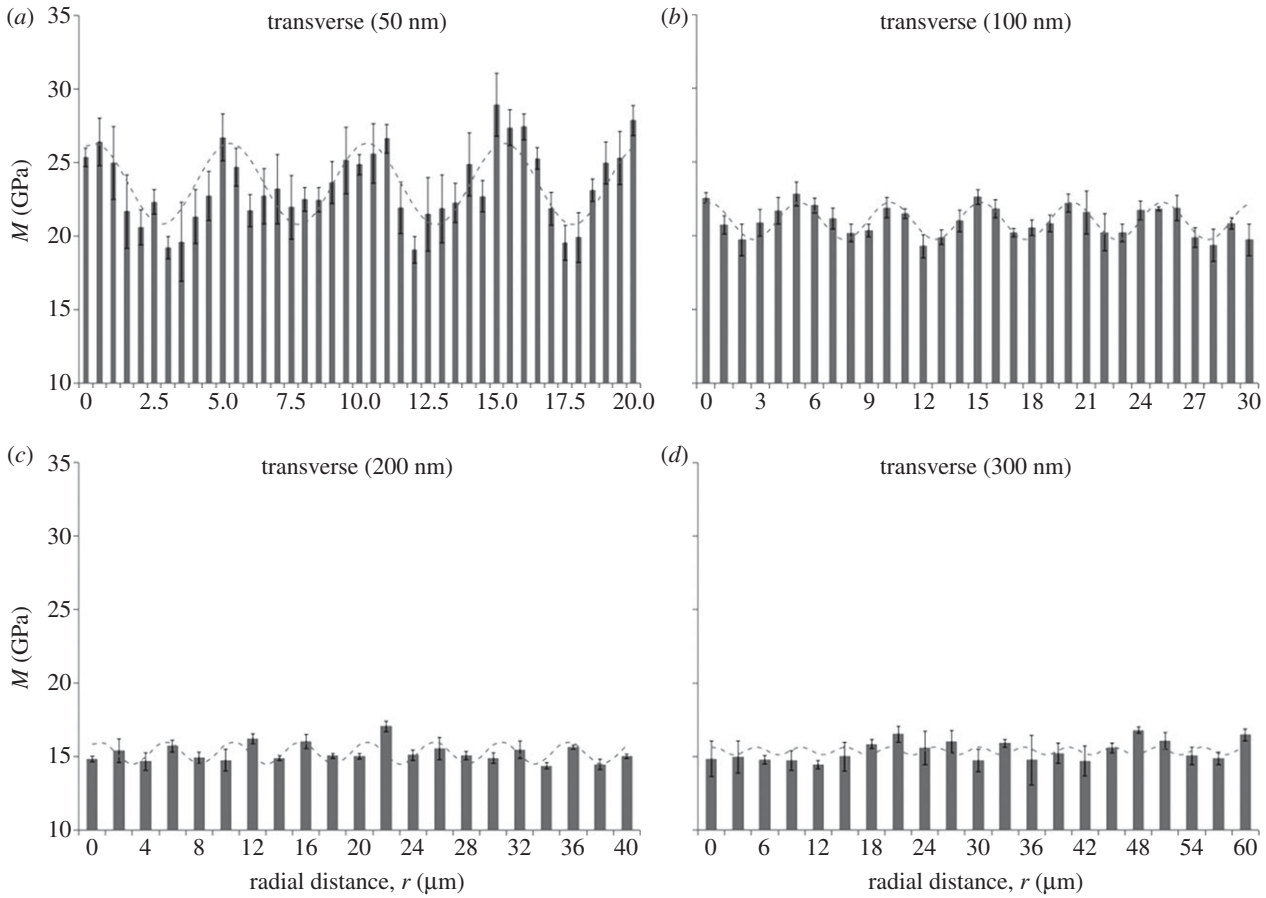

Figure 4. Spatial dependence of indentation modulus at (*a*) 50, (*b*) 100, (*c*) 200 and (*d*) 300 nm maximum penetration depth for transverse experiments (normal to the osteonal axis). Radial distance (*r*) begins at the Haversian canal edge. Each data point represents the mean value and standard deviation of a total of $n = 9$ measurements. The fitting to the oscillatory function of equation (2.1) is shown in each plot (dashed line). The coefficient of determination (R^2) values are (*a*) 0.61, (*b*) 0.58, (*c*) 0.61, and (*d*) 0.01. Note ordinate does not start at zero.

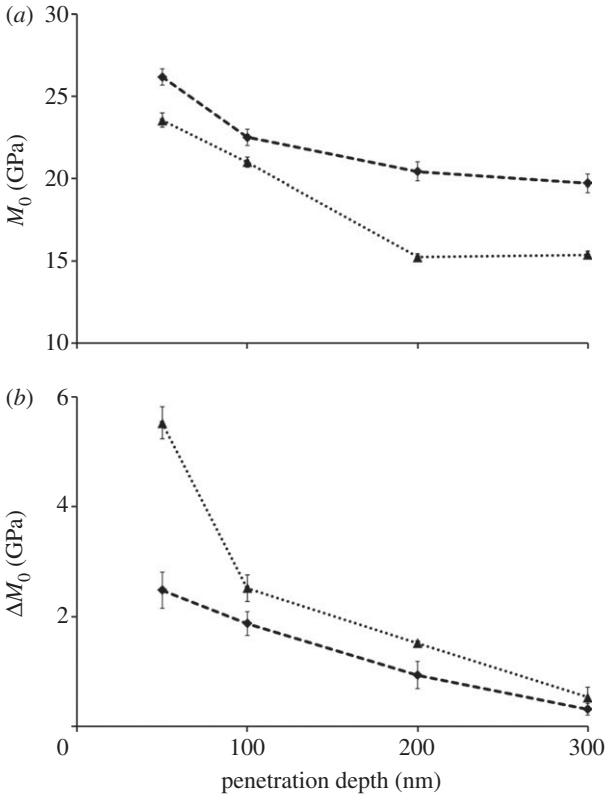

Figure 5. (*a*) Indentation modulus mean value and (*b*) amplitude trends with respect to penetration depth in the axial (dashed line with diamond) and transverse (dotted line with triangle) directions calculated from equation (2.1). Standard deviations refer to $n = 9$ measurements.

constants $\nu_{PP}(r_i)$, $\nu_{LP}(r_i)$ and $G_{LP}(r_i)$ were set to

$$\nu_{PP}(r_i) = 0.358; \quad \nu_{LP}(r_i) = 0.315;$$
$$\text{and} \quad G_{LP}(r)_i = \frac{E_L(r_i) + E_P(r_i)}{2} \times \frac{1}{2 \times (1 + ((\nu_{LP}(r_1) + \nu_{PL}(r_1))/2))}. \tag{3.1}$$

Here, $\nu_{PP}(r_i)$ and $\nu_{LP}(r_i)$ are average values from literature [18] and refer to the mechanical properties of a single sub-lamella. This procedure was applied to the nine couples of indentation moduli $M_A(r_i)$ and $M_T(r_i)$, enabling the identification of the nine corresponding couples of uniaxial elastic moduli $E_L(r_i)$ and $E_P(r_i)$ reported in figure 6*a*,*b* (bars).

The analytical model in equation (2.2) was then adopted to calculate $E(\theta)$ in the axial and transverse directions (figure 6*a*,*b*, sinusoidal curves), thus allowing the prediction of the stiffness at any arbitrary angle with respect to the fibril axis for the two experimental trends. In both cases, the Poisson's ratio ν_{LP} was set to the corresponding literature values for a sub-layer in an osteonal lamella found by Yoon & Cowin [18]; also, the periodicity of the modulation was set to the experimentally observed lamellar width (5.01 μm). Results of this fitting are provided in table 3. The small discrepancy (approx. 6%) in E_L between the axial and transverse directions means that the mineralized collagen fibrils belonging to the thick and thin sub-lamellae maintain similar longitudinal mechanical properties. E_P exhibited a much higher discrepancy between axial and transverse direction

Table 3. Results of fitting with equation (2.2) [19,26,27] independently applied to the 50 nm maximum depth data in terms of uniaxial elastic moduli E (figure 7) in the axial and transverse directions. The υ_{LP} values (bold typed) were assumed from Yoon & Cowin [18] to perform the fitting. The coefficient of determination R^2 is given in the last column.

indentation direction	E_L (GPa)	E_P (GPa)	G_{LP} (GPa)	υ_{LP} (−)	R^2 (−)
axial	27.70	22.60	9.26	**0.301**	0.88
transverse	26.17	17.98	8.16	**0.330**	0.86

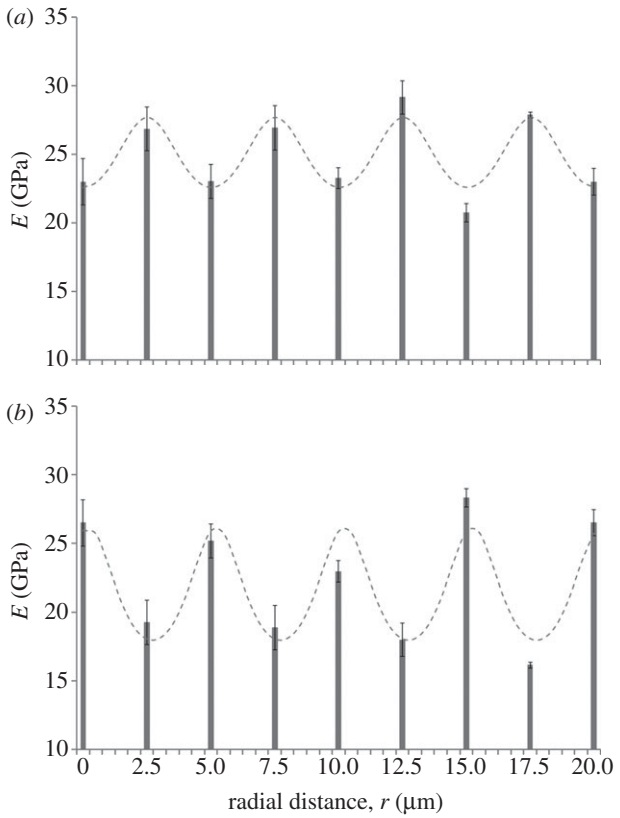

Figure 6. Spatial modulation (bars) of the uniaxial elastic moduli E obtained by using the Delafargue–Ulm approach [31] at 50 nm maximum penetration depth in the axial (*a*) and transverse (*b*) directions. Maxima correspond to E_L (longitudinal to collagen fibril long axis) and minima correspond to E_P (transverse to collagen fibril long axis). Standard deviations refer to $n = 9$ measurements. Fitting with the analytical model in equation (2.2) is also shown: the fitting results, together with the coefficient of determination values R^2, are reported in table 3. Note ordinate does not start at zero.

(approx. 23%), indicating that the transverse properties of the mineralized collagen fibrils are different in the thick and thin sub-lamellae.

3.3. Elastic constants for a sub-layer within an osteonal lamella

A set of orthotropic elastic parameters for a mineralized collagen fibrils sub-layer was inferred from the previous fittings by properly merging the two datasets reported in table 3. In the proposed set of elastic parameters (table 4), the uniaxial Young's modulus E_L corresponds to the mean value of the Young's moduli evaluated along the fibrils long axis in thin and thick layers; instead, uniaxial Young's moduli E_{P1} and E_{P2}, as well as the shear moduli G_{LP1} and G_{LP2}, are directly obtained from the previous fittings. The remaining entries of the stiffness tensor, i.e. the shear modulus and the Poisson's ratio in the P_1–P_2 plane, G_{P1P2} and υ_{P1P2}, were taken from literature [18]. For comparison purposes, the set of orthotropic elastic for a sub-layer in an osteonal lamella obtained by Yoon & Cowin [18] are included in table 4.

3.4. Validation of the experimental and analytical procedures

In order to validate the above procedure, the indentation moduli trends in the axial and transverse directions at 50 nm depth were calculated through the Swadener–Pharr method [32] using the set of elastic parameters reported in table 3 (transversely isotropic model) and in table 4 (orthotropic model). The indentation moduli are computed using 5° spacing for θ, corresponding to approximately 140 nm spacing in the radial paths. The computed values, compared with the experimental measures obtained at 50 nm maximum depth (figures 3*a* and 4*a*) and the fitting to the oscillatory function of equation (2.1), are shown in figure 7. Both material models agree reasonably well with the experimental values, as evidenced by the coefficients of determination R^2 (reported in figure 7 caption) ranging between 0.59 and 0.62.

Results from the application of the Swadener–Pharr method are also presented in tables 5 and 6, where the indentation moduli mean value and amplitude of the modulation calculated with the oscillatory function best fitting the data (see eq. (2.1)) are compared with the computed mean value and amplitude of the oscillatory trends (dotted lines in figure 7). The percentage differences between the experimental and the computed indentation values are lower for the orthotropic elastic behaviour (below 5%) than the transversely isotropic behaviour, where differences up to approximately 20 per cent were found. The two pieces of evidence above—i.e. the fact that the coefficient of determination R^2 associated to the Swadener–Pharr prediction with an orthotropic material model is similar to the R^2 values obtained via equation (2.1), and the low discrepancy in terms of indentation moduli mean value and amplitude of the modulation between the experimental and the computed data for and orthotropic model—support both the reliability of the elastic parameters obtained through application of equation (2.2) to the data and the assumption of orthotropy to model the elastic mechanical behaviour of a sub-layer of mineralized collagen fibrils within an osteonal lamella.

4. Discussion

The aim of the study was to determine the orientation and size-dependent mechanical properties of individual secondary osteons in cortical bone, as well as to investigate the

Table 4. Set of orthotropic elastic parameters for a sub-layer of mineralized collagen fibrils within an osteonal lamella, inferred by properly merging the two datasets in the axial and transverse directions reported in table 3. The $G_{P_1P_2}$, $\upsilon_{P_1P_2}$, υ_{LP_1} *and* υ_{LP_2} parameters (bold typed) were assumed from Yoon & Cowin [18]. For comparison purposes, the set of orthotropic elastic parameters for one sub-layer of the lamellar unit obtained by Yoon & Cowin [18] is reported also. The relationships $E_L > E_{P2} > E_{P1}$ and $\nu_{P_2P_1} > \nu_{P_2L} > \nu_{P_1L}$ are maintained, as well as $G_{LP_2} > G_{LP_1}$.

	E_{P1} (GPa)	E_{P2} (GPa)	E_L (GPa)	G_{P1P2} (GPa)	G_{LP1} (GPa)	G_{LP2} (GPa)
present work	17.98	22.60	26.94	**7.2**	8.16	9.26
Yoon & Cowin [18]	16.40	18.07	22.80	7.2	7.1	8.4
	ν_{P1P2} (−)	ν_{P2P1} (−)	ν_{P1L} (−)	ν_{P2L} (−)	ν_{LP1} (−)	ν_{LP2} (−)
present work	**0.334**	0.420	0.220	0.253	**0.330**	**0.301**
Yoon & Cowin [18]	0.334	0.381	0.237	0.247	0.330	0.301

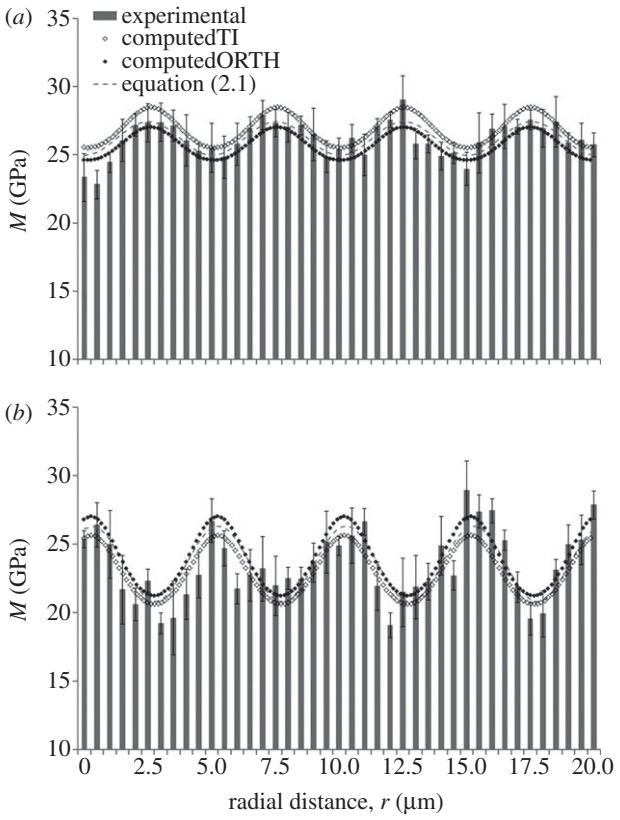

Figure 7. Comparison between the indentation moduli trends obtained experimentally (bars) and the ones computed with the Swadener–Pharr method [32] (dots) with a approximately 140 nm spacing in the (*a*) axial and (*b* transverse) directions. The fitting to the oscillatory function of equation (2.1) (dashed line) is shown as well. The input parameters for the Swadener–Pharr method are reported in tables 3 and 4 for transversely isotropic (TI) and orthotropic (ORTH) material models, respectively. In the axial direction (*a*), the coefficient of determination R^2 values are 0.59 and 0.60 for the transversely isotropic and orthotropic model, respectively; whereas, in the transverse direction (*b*), R^2 values are 0.62 and 0.61 for the transversely isotropic and orthotropic model, respectively. Note ordinate does not start at zero.

way the constituents' anisotropy and their arrangement in the hierarchical structure concur in the development of the anisotropic mechanical behaviour of the tissue. Indentation experiments at different maximum depths showed a periodic alternating of stiffer layers with less stiff layers in which the indentation modulus mean values, as well as the amplitude of the modulation depend on maximum depth and orientation of the indentation tests. A characteristic length owing to the periodicity of the osteonal lamellae was quantified. Further, the elastic constants for a sub-layer of mineralized collagen fibrils within an osteonal lamella were identified from the indentation moduli by applying an analytical model that assumes inherent anisotropy of the mineralized collagen fibrils as well as their spatial arrangement.

The smallest experimental characteristic length probed (50 nm maximum depth, approximately 400 nm contact diameter) is comparable to the size of a few mineralized collagen fibrils and allowed the evaluation of the mechanical properties of a single sub-layer of fibrils in the lamellar structure; whereas, the largest experimental characteristic length sampled (300 nm maximum depth, approx. 2 μm contact diameter) may accommodate approximately 10–20 bunches of collagen fibrils oriented along multiple directions and, thus, involves multiple sub-layers, whose thickness can vary between few hundreds of nanometres to a couple of microns [22,33–35]. These investigations enabled the identification of a decrease in the values of indentation moduli with the penetration depth (figure 5*a*) that indicates a possible size effect in the mechanical properties of cortical bone tissue. At the same time, decreasing values of amplitude ΔM (figure 5*b*) indicate that the indentation experiment is involving a sufficient amount of tissue volume such that homogenized material properties are sensed by the indentation probe. The stabilization of M_0 and the decay to a negligible value of ΔM occurs at approximately the same length scale. This suggests that the homogenization process has completely developed at approximately 300 nm maximum depth, corresponding to a approximately 2 μm contact diameter between the tissue and the indenter.

Homogenization arguments alone are not able to fully justify the pronounced decay of the indentation moduli with the penetration depth achieved with the experimental tests, quantifiable in approximately 24 per cent and approximately 34 per cent reductions in the axial and transverse directions, respectively. Instead, the decrease in indentation modulus with indentation depth may be explained by considering peculiar deformation and failure mechanisms of bone tissue at the nano-structural level, such as shear transfer between mineral particles via intermediate ductile organic layers [36], slippage at the collagen–mineral interface [37], phase transformation of the mineral phase [38] and sacrificial bond disruption between fibrils [39]. In particular, Gupta *et al*. [40,41] showed that critical interfacial shear strength between the fibril and the interfibrillar matrix layer is exceeded when the bone is compressed above the yield point. When this happens, the matrix flows past the fibrils,

Table 5. Comparison between the indentation moduli mean value and amplitude of the modulation calculated with the oscillatory function in equation (2.1) and computed by the Swadener–Pharr method [32] in the axial and transverse directions. Percentage discrepancies are calculated as $e_{M_0} = |M_0^{comp} - M_0^{eq.\ (2.1)}|/M_0^{eq.\ (2.1)}$ and $e_{\Delta M} = |\Delta M^{comp} - \Delta M^{equation\ (2.1)}|/\Delta M^{eq.\ (2.1)}$. The transversely isotropic material model is used.

indentation direction	$M_0^{eq.\ (2.1)}$ (GPa)	M_0^{comp} (GPa)	$\Delta M^{eq.\ (2.1)}$ (GPa)	ΔM^{comp} (GPa)	e_{M0}(%)	$e_{\Delta M}$ (%)
axial	26.19	27.00	2.48	2.97	3.07	19.76
transverse	23.56	23.15	5.53	5.01	−1.78	−9.40

Table 6. Comparison between the indentation moduli mean value and amplitude of the modulation calculated with the oscillatory function in equation (2.1) and computed by the Swadener–Pharr method [32] in the axial and transverse direction. Percentage discrepancies are calculated as in table 4. The orthotropic material model is used.

indentation direction	$M_0^{eq.\ (2.1)}$ (GPa)	M_0^{comp} (GPa)	$\Delta M^{eq.\ (2.1)}$ (GPa)	ΔM^{comp} (GPa)	e_{M0}(%)	$e_{\Delta M}$ (%)
axial	26.19	25.80	2.48	2.43	−1.51	−2.02
transverse	23.56	24.13	5.53	5.77	2.38	4.34

resulting in frictional losses and de-bonding of the fibrils and extrafibrillar matrix. A further evidence for this mechanism is achieved considering a single loading–unloading cycle of bone [41], as when a bone sample is relaxed after being deformed beyond the yield point, irreversible deformations develop at the tissue level but not at the fibril level. If we compare the loading and unloading stiffnesses at the tissue level, damage induced decrease in the tissue Young's modulus occurs: this decay, quantified as approximately 20–25%, is consistent with the progressive diminishing of the stiffness mean value while increasing the maximum depth evidenced in the present work. Moreover, as the deformation mechanisms mentioned above contribute in determining a loss of integrity of the tissue, they can be considered as damage phenomena that cause a progressive degradation of material continuity; we speculate that a damage model can phenomenologically represents the overall tissue response subject to nanoindentation. Recently, a numerical study performed by our group [42] was devoted to the investigation of the role played by damage mechanics in the nanoindentation of osteonal lamellar bone, and we showed that damage models can predict the loss in mechanical properties obtained in the experiments.

The results of this work show that the stiffness modulation of the tissue is consistent with anisotropic fibrillar layers with a specific crystal orientation. Indeed, based on the difference of the elastic moduli in the directions perpendicular to the fibril (E_P; table 3) between the thick and thin sub-lamellae, it can be speculated that the mineral platelets have an intrinsic orientation that could play a role in determining the mechanical properties normal to the fibrils long axis. This observation would agree with the rotated plywood model introduced by Weiner *et al.* [33,34], where collagen fibrils are rotated not only with respect to the lamellar boundary but also around their own axis (figure 8), as the mechanical properties obtained for a sub-layer can be explained by the azimuthal rotation of the fibrils around the longitudinal axis L, which changes the crystal orientation. Further evidence that the hydroxyapatite crystals strongly influence the elastic properties of the mineralized collagen fibrils along different directions is provided by Rho *et al.* [43], who studied intramuscular herring bones where mineralized collagen fibrils have a single orientation

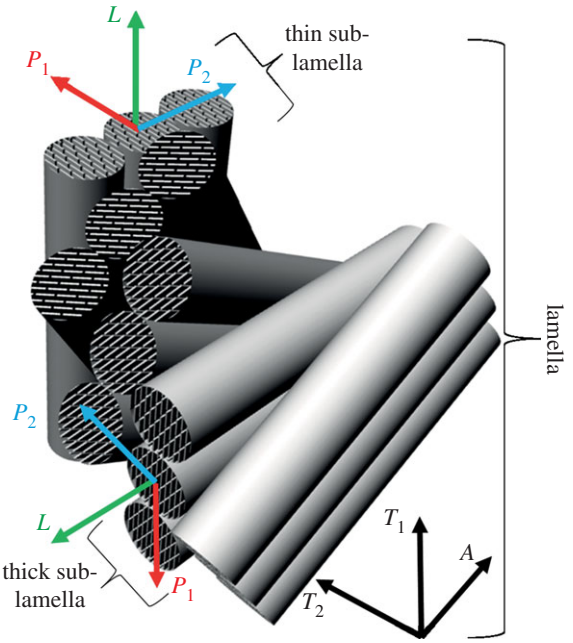

Figure 8. Schematic illustration of the organization of mineralized collagen fibrils and the plate-shaped mineral crystals within the fibrils in a lamellar unit of osteonal bone according to the rotated plywood model introduced by Weiner *et al.* [33,34]. The three local orthogonal reference axes labelled L, P_1 and P_2 (relative to the axis of an individual mineralized collagen fibril) are provided. The three global orthogonal reference axes A, T_1 and T_2 (relative to the osteonal axis) are provided too. Not drawn to scale. (Online version in colour.)

with a variation in mineralization along the length. Results clearly showed that the anisotropy ratio is influenced by the mineralization, as it drops from approximately 2.1 in the fully mineralized region to approximately 1.1 in areas at the earliest stage of mineralization. In this case, the presence of the mineral crystals seems to be the main aspect responsible for the difference in the elastic properties along different directions.

As already said in the §2, the bone samples were tested in ambient conditions. Although samples still retain a significant degree of hydration in this condition, in general an artificial increase in stiffness and reduction in ductility compared with the native state could results. However,

Hengsberger *et al.* [44] adopted instrumented indentation to compare dry and wet samples at different length scales, which are comparable to the ones investigated here. Basically, what they found is that: (i) thick lamellae exhibited a significant decrease in indentation modulus with increasing indentation depth, as reported in this study and (ii) the comparative trends of indentation depth and lamella type were similar for dry and physiological conditions. Thus, the effect of testing dry instead of wet samples seems the same at multiple length scales. Therefore, relative modulations in mechanical properties are expected to remain valid, as well as the comparison between the mechanical properties at the different experimental characteristic length probed and along different directions. Anyway, future developments will consider the application of the present experimental–analytical procedure to tests in conditions closer to the physiological ones.

5. Conclusion

In this work, the hierarchical arrangement of lamellar bone was found to be a major determinant for modulation of mechanical properties and anisotropic mechanical behaviour of the tissue. In more detail:

— the size effect on lamellar bone anisotropic mechanical behaviour, evidenced by the decline of indentation modulus versus probe size, and the critical length at which homogenization of the mechanical properties occurs were determined by measuring the spatial modulation of indentation response;

— by using a laminate-composite-based analytical model, the elastic constants for a sub-layer of mineralized collagen fibrils within an osteonal lamella were determined on the basis of their spatial arrangements and were validated through direct comparison of the experimental indentation moduli and the predicted ones computed by the Swadener–Pharr model.

The structural complexity of bone tissue requires that the assessment of its mechanical properties involves multiple hierarchical levels, from the macroscopic scale down to the micro- and nano-structural level till the most basic components. Understanding structure–property relationships and the effects of structural features on the biomechanical properties of bone would enable not only the development of more accurate models for analysis of implants and potential bone-replacement materials, but also the progress in designing bioinspired structural materials that take advantage of the mechanical design principles found in nature. These latter topics undoubtedly represent fascinating long-term scientific goals in the materials science and engineering field.

The authors would like to thank the MIT-Italy Programme for supporting the research and the Progetto Rocca for supporting Davide Carnelli's scholarship at the MIT. The DMSE Nanomechanical Technology Laboratory and the Institute for Soldier Nanotechnologies (ISN) at the MIT are gratefully acknowledged for use of equipment and facilities. M.D. acknowledges support by the ONR grant no. N00014-08-1-0510, and by the Advanced Materials for Micro and Nano Systems Programme of the Singapore-MIT Alliance (SMA).

References

1. Weiner S, Wagner HD. 1998 The material bone: structure mechanical function relations. *Annu. Rev. Mater. Sci.* **28**, 271–298. (doi:10.1146/annurev.matsci.28.1.271)
2. Currey JD. 2002 *Bones: structure and mechanics*. Princeton, NJ: Princeton University Press.
3. Cowin SC. 2001 *Bone mechanics handbook*. Boca Raton, FL: CRC Press Inc.
4. Currey JD. 1984 *The mechanical adaptations of bones*. Princeton, NJ: Princeton University Press.
5. Rho JY, Kuhn-Spearing L, Zioupos P. 1998 Mechanical properties and the hierarchical structure of bone. *Med. Eng. Phys.* **20**, 92–102. (doi:10.1016/S1350-4533(98)00007-1)
6. Fratzl P, Weinkamer R. 2007 Nature's hierarchical materials. *Prog. Mater. Sci.* **52**, 1263–1334. (doi:10.1016/j.pmatsci.2007.06.001)
7. Fratzl P, Gupta HS, Paschalis EP, Roschger P. 2004 Structure and mechanical quality of the collagen-mineral nano-composite in bone. *J. Mater. Chem.* **14**, 2115–2123. (doi:10.1039/B402005G)
8. Fratzl P, Gupta HS. 2007 *Nanoscale mechanisms of bone deformation and fracture*. Weinheim, Germany: Wiley-VCH Verlag GmbH.
9. Wagermaier W, Gupta HS, Gourrier A, Burghammer M, Roschger P, Fratzl P. 2006 Spiral twisting of fiber orientation inside bone lamellae. *Biointerphases* **1**, 1–5. (doi:10.1116/1.2178386)
10. Wagermaier W, Gupta HS, Gourrier A, Paris O, Roschger P, Burghammer M, Riekel C, Fratzl P. 2007 Scanning texture analysis of lamellar bone using microbeam synchrotron X-ray radiation. *J. Appl. Crystall.* **40**, 115–120. (doi:10.1107/S0021889806044888)
11. Reilly DT, Burstein AH. 1975 The elastic and ultimate properties of compact bone tissue. *J. Biomech.* **6**, 393–396. (doi:10.1016/0021-9290(75)90075-5)
12. Ascenzi A, Baschieri P, Benvenuti A. 1994 The torsional properties of single selected osteons. *J. Biomech.* **27**, 875–884. (doi:10.1016/0021-9290(94)90260-7)
13. Ascenzi A, Ascenzi MG, Benvenuti A, Mango F. 1997 Pinching in longitudinal and alternate osteons during cyclic loading. *J. Biomech.* **30**, 689–695. (10.1016/S0021-9290(97)00002-X)
14. Rho JY. 1996 An ultrasonic method for measuring the elastic properties of human tibial cortical and cancellous bone. *Ultrasonics* **34**, 777–783. (doi:10.1016/S0041-624X(96)00078-9)
15. Fan Z, Swadener JG, Rho JY, Roy ME, Pharr GM. 2002 Anisotropic properties of human tibial cortical bone as measured by nanoindentation. *J. Orthop. Res.* **20**, 806–810. (doi:10.1016/S0736-0266(01)00186-3)
16. Rho JY, Currey JD, Zioupos P, Pharr GM. 2001 The anisotropic young's modulus of equine secondary osteones and interstitial bone determined by nanoindentation. *J. Exp. Biol.* **204**, 1775–1781.
17. Franzoso G, Zysset PK. 2009 Elastic anisotropy of human cortical bone secondary osteons measured by nanoindentation. *J. Biomech. Eng.* **131**, 021001.1–021001.11. (doi:10.1115/1.3005162)
18. Yoon YJ, Cowin SC. 2008 The estimated elastic constants for a single bone osteonal lamella. *Biomech. Model. Mechanobiol.* **7**, 1–11. (doi:10.1007/s10237-006-0072-8)
19. Gupta HS, Stachewicz U, Wagermaier W, Roschger P, Wagner HD, Fratzl P. 2006 Mechanical modulation at the lamellar level in osteonal bone. *J. Mater. Res.* **21**, 1913–1921. (doi:10.1557/jmr.2006.0234)
20. Kasiri S, Taylor D. 2008 A critical distance study of stress concentrations in bone. *J. Biomech.* **41**, 603–609. (doi:10.1016/j.jbiomech.2007.10.003)
21. Yao H, Dao M, Carnelli D, Tai K, Ortiz C. 2011 Size-dependent heterogeneity benefits the mechanical performance of bone. *J. Mech. Phys. Solid* **59**, 64–74. (doi:10.1016/j.jmps.2010.09.012)

22. Hofmann T, Heyroth F, Meinhard H, Franzel W, Raum K. 2006 Assessment of composition and anisotropic elastic properties of secondary osteon lamellae. *J. Biomech.* **39**, 2282–2294. (doi:10.1016/j.jbiomech.2005.07.009)
23. Oliver WC, Pharr GM. 2004 Measurement of hardness and elastic modulus by instrumented indentation: advances in understanding and refinements to methodology. *J. Mater. Res.* **19**, 3–20. (doi:10.1557/jmr.2004.19.1.3)
24. Tai K, Qi HJ, Ortiz C. 2005 Effect of mineral content on the nanoindentation properties and nanoscale deformation mechanisms of bovine tibial cortical bone. *J. Mater. Sci. Mater. Med.* **16**, 947–959. (doi:10.1007/s10856-005-4429-9)
25. Oliver WC, Pharr GM. 1992 An improved technique for determining hardness and elastic modulus using load and displacement sensing indentation experiments. *J. Mater. Res.* **7**, 1564–1583. (doi:10.1557/JMR.1992.1564)
26. Currey JD. 1969 The relationship between the stiffness and the mineral content of bone. *J. Biomech.* **2**, 477–480. (doi:10.1016/0021-9290(69)90023-2)
27. Seto J, Gupta HS, Zaslansky P, Wagner HD, Fratzl P. 2008 Tough lessons from bone: extreme mechanical anisotropy at the mesoscale. *Adv. Funct. Mater.* **18**, 1905–1911. (doi:10.1002/adfm.200800214)
28. Fritsch A, Hellmich C. 2007 Universal microstructural patterns in cortical and trabecular, extracellular and extravascular bone materials: micromechanics-based prediction of anisotropic elasticity. *J. Theor. Biol.* **244**, 597–620. (doi:10.1016/j.jtbi.2006.09.013)
29. Hellmich C, Ulm FJ. 2002 Are mineralized tissues open crystal foams reinforced by crosslinked collagen? Some energy arguments. *J. Biomech.* **35**, 1199–1212. (doi:10.1016/S0021-9290(02)00080-5)
30. Hellmich C, Barthélémy J-F, Dormieux L. 2004 Mineral–collagen interactions in elasticity of bone ultrastructure-a continuum micromechanics approach. *Eur. J. Mech. A Solids* **23**, 783–810. (doi:10.1016/j.euromechsol.2004.05.004)
31. Delafargue A, Ulm FJ. 2004 Explicit approximations of the indentation modulus of elastically orthotropic solids for conical indenters. *Int. J. Solids Struct.* **41**, 7351–7360. (doi:10.1016/j.ijsolstr.2004.06.019)
32. Swadener JG, Pharr GM. 2001 Indentation of elastically anisotropic half-spaces by cones and parabolas of revolution. *Phil. Mag. A* **81**, 447–466. (doi:10.1080/01418610108214314)
33. Weiner S, Arad T, Sabanay I, Traub W. 1997 Rotated plywood structure of primary lamellar bone in the rat: orientations of the collagen fibril arrays. *Bone* **20**, 509–514. (doi:10.1016/S8756-3282(97)00053-7)
34. Weiner S, Traub W, Wagner HD. 1999 Lamellar bone: structure–function relations. *J. Struct. Biol.* **126**, 241–255. (doi:10.1006/jsbi.1999.4107)
35. Akiva U, Wagner HD, Weiner S. 1998 Modelling the three-dimensional elastic constants of parallel-fibred and lamellar bone. *J. Mater. Sci.* **33**, 1497–1509. (doi:10.1023/A:1004303926771)
36. Jager I, Fratzl P. 2000 Mineralized collagen fibrils: a mechanical model with a staggered arrangement of mineral particles. *Biophys. J.* **79**, 1737–1746. (doi:10.1016/S0006-3495(00)76426-5)
37. Mercer C, He MY, Wang R, Evans AG. 2006 Mechanisms governing the inelastic deformation of cortical bone and application to trabecular bone. *Acta Biol.* **2**, 59–68. (doi:10.1016/j.actbio.2005.08.004)
38. Carden A, Rajachar RM, Morris MD, Kohn DH. 2003 Ultrastructural changes accompanying the mechanical deformation of bone tissue: a raman imaging study. *Calcif. Tissue Int.* **72**, 166–175. (doi:10.1007/s00223-002-1039-0)
39. Fantner G *et al*. 2005 Sacrificial bonds and hidden length dissipate energy as mineralized fibrils separate during bone fracture. *Nat. Mater.* **4**, 612–616. (doi:10.1038/nmat1428)
40. Gupta HS, Wagermaier W, Zickler GA, Aroush DRB, Funari SS, Roschger P, Wagner HD, Fratzl P. 2005 Nanoscale deformation mechanisms in bone. *Nano Lett.* **5**, 2108–2111. (doi:10.1021/nl051584b)
41. Gupta HS, Wagermaier W, Zickler GA, Hartmann J, Funari SS, Roschger P, Wagner HD, Fratzl P. 2006 Fibrillar level fracture in bone beyond the yield point. *Int. J. Fracture* **139**, 425–436. (doi:10.1007/s10704-006-6635-y)
42. Lucchini R, Carnelli D, Ponzoni M, Bertarelli E, Gastaldi D, Vena P. 2011 Role of damage mechanics in nanoindentation of lamellar bone at multiple sizes: experiments and numerical modeling. *J. Mech. Behav. Biomed. Mater.* **4**, 1852–1863. (doi:10.1016/j.jmbbm.2011.06.002)
43. Rho JY, Mishra SR, Chung K, Bai J, Pharr GM. 2001 Relationship between ultrastructure and the nanoindentation properties of intramuscular herring bones. *Ann. Biomed. Eng.* **29**, 1082–1088. (doi:10.1114/1.1424913)
44. Hengsberger S, Kulik A, Zysset P. 2002 Nanoindentation discriminates the elastic properties of individual human bone lamellae under dry and physiological conditions. *Bone* **30**, 178–184. (doi:10.1016/S8756-3282(01)00624-X)